Cite as: M. Saliba *et al.*, *Science*
10.1126/science.aah5557 (2016).

Incorporation of rubidium cations into perovskite solar cells improves photovoltaic performance

Michael Saliba,[1]*† Taisuke Matsui,[1,2]* Konrad Domanski,[1]* Ji-Youn Seo,[1] Amita Ummadisingu,[1] Shaik M. Zakeeruddin,[1] Juan-Pablo Correa-Baena,[3] Wolfgang R. Tress,[1] Antonio Abate,[1] Anders Hagfeldt,[3] Michael Grätzel[1]†

[1]Laboratory of Photonics and Interfaces, École Polytechnique Fédérale de Lausanne, Station 6, CH-1015 Lausanne, Switzerland. [2]Advanced Research Division, Materials Research Laboratory, Panasonic Corporation, 1006 Kadoma, Kadoma City, Osaka 571-8501, Japan. [3]Laboratory of Photomolecular Science, École Polytechnique Fédérale de Lausanne, Station 6, CH-1015 Lausanne, Switzerland.

*These authors contributed equally to this work.

†Corresponding author. E-mail: michael.saliba@epfl.ch (M.S.); michael.graetzel@epfl.ch (M.G.)

All of the cations currently used in perovskite solar cells (PSCs) abide by the tolerance factor for incorporation into the lattice. We show that the small and oxidation-stable Rb^+ can be embedded into a "cation cascade" to create perovskite materials with excellent material properties. We achieved stabilized efficiencies of up to 21.6% (average value: 20.2%) on small areas (and a stabilized 19.0% on a 0.5 cm^2 cell) as well as an electroluminescence of 3.8%. The open-circuit voltage of 1.24 volts at a band gap of 1.63 electron volts leads to loss-in-potential of 0.39 V, versus 0.4 V for commercial silicon cells. Polymer-coated cells maintained 95% of their initial performance at 85°C for 500 hours under full solar illumination and maximum power point tracking.

Low-cost perovskite solar cells (PSCs) have achieved certified power conversion efficiencies (PCEs) of 22.1% (*1*). The organic-inorganic perovskites used for photovoltaics (PV) have an AMX_3 formula that is comprised of a monovalent cation, A = [cesium Cs^+; methylammonium (MA) $CH_3NH_3^+$; formamidinium (FA) $CH_3(NH_2)_2^+$]; a divalent metal M = (Pb^{2+}; Sn^{2+}); and an anion X = (Cl^-, Br^-; I^-). The highest efficiency perovskites are Pb-based with mixed MA/FA cations and Br/I halides (*2*–*4*). Recently, Cs was used to explore more complex cation combinations, i.e., Cs/MA, Cs/FA and Cs/MA/FA (*5*–*9*). These perovskite formulations exhibit unexpected properties. For example, Cs/FA mixtures supress halide segregation enabling band gaps for perovskite/silicon tandems (*10*). The Cs/MA/FA based solar cells are more reproducible and thermally stable than MA/FA mixtures (*9*).

In general, increasing the perovskite complexity is motivated by the need to improve stability by adding more inorganic elements and increasing the entropy of mixing, which can stabilize ordinarily unstable materials (such as the "yellow," non-photoactive phase of $FAPbI_3$ that can be avoided using small amounts of the otherwise unstable $CsPbI_3$) (*6*, *7*). However, all combinations of Cs, MA, and FA cations were selected because each individually forms a photoactive perovskite "black" phase (*11*–*13*).

In order to progress further, a wider circle of cations need to be explored. However, most monovalent cations are mismatched to sustain a photoactive $APbI_3$ perovskite with an appropriate Goldschmidt tolerance factor [$t = r_A + r_I / \sqrt{2}(r_{Pb} + r_I)$; r are the respective ionic radii] between 0.8 and 1.0 (*14*) rendering almost all elemental cations too small for consideration. We illustrate this point in Fig. 1A where we conduct tolerance factor calculations for the alkali metals (Li, Na, K, Rb, Cs); and MA, FA (see table S1 for the numeric values and ionic radii). We selected specifically the alkali metals which are oxidation-stable monovalent cations, as these would have a stability advantage over oxidation-prone Pb/Sn mixtures that have distorted material electronic properties (*15*).

The tolerance factor shows that only $CsPbI_3$ (as well as $MAPbI_3$ and $FAPbI_3$) fall into the range of "established perovskites" with a black phase. However, while Li, Na and K are clearly outside of the range, $RbPbI_3$ only misses by a small margin. The ionic radius of Cs and Rb is 167 pm and 152 p.m., respectively. This small difference still has a large impact, with $RbPbI_3$ and $CsPbI_3$ drawing the demarcation line between photoactive black perovskite and photoinactive yellow non-perovskite phases. In Fig. 1B, we demonstrate this by heating $CsPbI_3$ and $RbPbI_3$ films at different temperatures. Both films are yellow at 28°C. Upon heating to 380°C, only $CsPbI_3$ turns black whereas $RbPbI_3$ remains yellow. Finally, at 460°C both films start melting irreversibly without $RbPbI_3$ ever showing a black phase which is consistent with the observations by Trots and co-workers (*16*).

Thus, only $CsPbI_3$ has a black phase explaining why Rb, despite its desirable oxidation stability, has so far not been used for PSCs.

In this work, we propose embedding Rb^+, only slightly smaller than Cs^+, into a photoactive perovskite phase using multiple A-cation formulations. We retain FA as the majority cation because of the beneficial, red-shifted band gap. We identify four previously unexplored combinations: RbFA; RbCsFA, RbMAFA; and RbCsMAFA. In (*17*) and figs. S1 to S3, following the antisolvent approach pioneered by Jeon *et al.* (*2*), we present device data on a glass/fluorine-doped tin oxide/compact TiO_2/mesoporous TiO_2/perovskite/spiro-OMeTAD/Au architecture [see fig. S4A for a cross sectional scanning electron microscopy (SEM) image and fig. S4C for an image of typical devices]. All preparation details are given in (*17*). We use the nomenclature of RbFA, RbCsFA, RbMAFA, and RbCsMAFA to denote the entire perovskite compounds at the optimized values found in (*17*) (usually achieved with an addition of 5 to 10% Rb).

Reasonable device performances were reached with RbFA (14%), RbCsFA (19.3%), RbMAFA (19.2%) comparable to CsFA (20%), CsMAFA (19.2%), as shown in figs. S1 to S3 (measured on a device area of 0.16 cm^2). Thus, Rb can stabilize the black phase of FA perovskite and be integrated into PSCs, despite not being suitable as a pure $RbPbI_3$ compound. Surprisingly, RbCsMAFA (with 5% of Rb, fig. S3) results in PCEs of 20.6% [with an open-circuit voltage (V_{oc}) of 1186 mV] (*17*). Hence, we focus below on RbCsMAFA in order to substantiate the impact of Rb^+ integration approach for PSCs.

We investigated the starting condition of the crystallization process for the RbCsMAFA compound upon annealing at 100°C, which is needed to fully crystallize the perovskite films. In Fig. 2A, we present the ultraviolet-visible (UV-vis) and photoluminescence (PL) data of the unannealed MAFA and RbCsMAFA films. Whereas MAFA showed several PL peaks with maxima ranging from 670 to 790 nm, the RbCsMAFA film had a narrow peak at 770 nm attributable to perovskite. The insets are fluorescence microscopy maps of the surface of the unannealed films showing that the MAFA films are comprised of various emissive species forcing the pre-annealed film to crystallize with inhomogeneous starting conditions. However, the RbCsMAFA films were emissive in a narrow range and begin to crystallize from more homogeneous conditions. Thus, the addition of the inorganic cations enforced a crystallization that starts with a photoactive perovskite phase (near the final emission after annealing) instead of a mixture of varying emissions that need to converge toward the final emission (see Fig. 2C). These results are consistent with the high reproducibility and lack of yellow phase in the RbCsMAFA films.

Furthermore, we collected the corresponding x-ray diffraction (XRD) data of the unannealed films (Fig. 2B) that showed a pronounced perovskite peak for RbCsMAFA as compared to MAFA films. In Fig. 2, C and D, we show analogous data after annealing including UV-vis, PL and XRD data revealing a RbCsMAFA band gap of ~1.63 eV (slightly blue shifted compared to MAFA at ~1.62 eV) containing neither a PbI_2 nor a yellow δ-phase peak. The low-angle perovskite peak for MAFA and RbCsMAFA occurs at 14.17° and 14.25°, respectively, revealing that Rb indeed modified the crystal lattice. In figs. S5 and S6, we show XRD data of RbMAFA perovskite where we increased the concentration of Rb. We observed, similar to CsMAFA (*9*), that the lead excess and the yellow-phase impurities of MAFA perovskite disappeared when Rb was added. For Rb_5MAFA, there was a shift to wider angles for the perovskite peak. Moreover, in figs. S7 and S8, we show a series of RbCsMAFA perovskite with an increased amount of Rb together with a $RbPbI_3$ reference. We observed that the perovskite peak shifted to wider angles for Rb_5CsMAFA as well as further suppression of the residual PbI_2 (12.7°) and yellow-phase peak (11.7°) of FA-perovskite. Interestingly, as more Rb was added, we noted the appearance of a second peak at 13.4° and a double peak at 10.1° which coincide with the peaks for the pure yellow-phase $RbPbI_3$ indicating phase segregation at higher Rb concentrations. This is in good agreement with previous work where a phase segregation was also observed as more and more Cs was added to FA-based perovskite (*8*).

In addition, the top-view scanning electron microscopy (SEM) images reveal large crystals in the RbCsMAFA devices (see fig. S9), which has been shown to be beneficial for the PV metrics (*18*). We also show energy-dispersive X-ray spectroscopy measurements in fig. S10 indicating the presence and distribution of Cs and Rb within the perovskite layer.

We collected statistical data on RbCsMAFA devices (with 12 CsMAFA and 17 RbCsMAFA devices measured with a scan rate of 10 mV s^{-1} without preconditioning, such as light soaking or long-term forward voltage biasing; see fig. S11) and observed superior performance compared to CsMAFA. Remarkably, the average open-circuit voltage (V_{oc}) is increased from 1120 to 1158 mV and the fill factor from 0.75 to 0.78. In Fig. 3A, we show the RbCsMAFA champion cell reached a stabilized power output of 21.6% with a fill factor of 81% and 1180 mV open-circuit voltage. The measured J_{sc} matched the incident-photon-to-current-efficiency (IPCE) measurement in fig. S12. We also achieved a stabilized PCE of 19.0% on a large-area 0.5 cm^2 device (see fig. S13).

To correctly determine the V_{oc}, we investigated RbCsMAFA devices with the active area being fully illuminated, held at room temperature, and under an inert nitrogen atmosphere. This setup permitted an accurate V_{oc} value without heating or degradation effects (from moisture for example). In Fig. 3B, for one of our highest performing devices, we measured an outstanding V_{oc} of 1240 mV confirmed by the inset that is tracking the V_{oc} over time. The "loss-in-potential" (difference between V_{oc} and band gap) is only ~0.39 V, which is one of the lowest recorded for any PV material, implying very small non-radiation recombination losses (*19*). The high V_{oc} is particularly intriguing because this is the major parameter preventing PSCs from reaching their thermodynamic limit (J_{sc} and FF are already approaching their maximal values). Theoretically, in very pure, defect-free materials with only radiative recombination, the loss-in-potential can be as small as 0.23 (band gap of 1 eV) to 0.3 V (band gap of 2 eV). In particular, silicon, the main industrial PV material, cannot approach this limit because of its indirect band gap and Auger recombination exhibiting a loss-in-potential of ~0.4 V for the most efficient devices (*19*).

The non-radiative recombination losses were quantified by measuring the external electroluminescence quantum efficiency (EQE_{EL}), which is > 1% at a driving current that is equal to the short circuit current (see Fig. 3C). This value is in the same order of magnitude and thus consistent with a measured external PL quantum yield of 3.6% for RbCsMAFA (and 2.4% for CsMAFA). Following the approach in (*20*–*24*) [see also fig. S14 and (*17*)], we used the EQE_{EL} and the emission spectrum to predict a V_{oc} of 1240 mV confirming independently the value measured from the JV curve.

Furthermore, for higher driving currents, the EQE_{EL} in Fig. 3C reaches 3.8%, making the solar cell one of the most efficient perovskite LEDs as well, emitting in the near IR/red spectral range (see inset image) (*25*–*27*). We also present a video in the SM showing a RbCsMAFA device mounted in our custom-made device holder. As we tuned toward maximum emission and back, we observed bright EL in day light. For comparison, for commercially available Si solar cells, $EQE_{EL} \approx 0.5\%$ (*19*). These values for our PSC devices indicates that all major sources of non-radiative recombination were strongly suppressed and the material has very low bulk and surface defect density. We also investigate transport behavior using intensity-modulated photocurrent spectroscopy (IMPS) suggesting that the charge transport within the RbCsMAFA perovskite layer is substantially faster than in CsMAFA which is already much more defect-free compared to MAFA (*18*) [see also fig. S15 and (*17*)].

Despite the high efficiencies and an outstanding EL, this Rb-containing perovskite material must be able achieve high stability. This task is not trivial given the hygroscopic nature of perovskite films, phase instabilities and light sensitivity (*28*). Interestingly, the Achilles' heel of PSCs is not necessarily the perovskite itself but rather the commonly used 2,2′,7,7′-tetrakis(N,N-di-p-methoxyphenylamine)-9,9′-spirobifluorene (spiro-OMeTAD) hole transporter material (HTM) that becomes permeable (at elevated temperature) to metal electrode diffusion into the perovskite causing irreversible degradation (*29*, *30*). This effect can be mitigated with buffer layers or by avoiding the usage of metal electrodes (*29*–*31*). Alternatively, for the combined heat-light stress tests in this work, we find a thin layer of PTAA (see SEM image in fig. S4B) to work equally well (*32*). We imposed the above protocols simultaneously and aged devices for 500 hours at 85°C under continuous illumination with full solar intensity and maximum power point tracking in a nitrogen atmosphere. This compounded stress test exceeds industrial standards (*33*). We show the result in Fig. 3D (red curve, circles). The device started with > 17% efficiency at room temperature before the aging protocol was applied (see fig. S16 for a non-normalized PCE, FF, J_{sc}, V_{oc}, J_{MPP} and V_{MPP}). During the 85°C step (in which the V_{oc} is inevitably lowered), the device retained 95% of its initial performance.

REFERENCES AND NOTES

1. National Renewable Energy Laboratory, Best Research-Cell Efficiencies chart; www.nrel.gov/ncpv/images/efficiency_chart.jpg.
2. N. J. Jeon, J. H. Noh, W. S. Yang, Y. C. Kim, S. Ryu, J. Seo, S. I. Seok, Compositional engineering of perovskite materials for high-performance solar cells. *Nature* **517**, 476–480 (2015). Medline doi:10.1038/nature14133
3. M. Saliba, S. Orlandi, T. Matsui, S. Aghazada, M. Cavazzini, J.-P. Correa-Baena, P. Gao, R. Scopelliti, E. Mosconi, K.-H. Dahmen, F. De Angelis, A. Abate, A. Hagfeldt, G. Pozzi, M. Graetzel, M. K. Nazeeruddin, A molecularly engineered hole-transporting material for efficient perovskite solar cells. *Nat. Energy* **1**, 15017 (2016). doi:10.1038/nenergy.2015.17
4. X. Li, D. Bi, C. Yi, J. D. Décoppet, J. Luo, S. M. Zakeeruddin, A. Hagfeldt, M. Grätzel, A vacuum flash-assisted solution process for high-efficiency large-area perovskite solar cells. *Science* **353**, 58–62 (2016). Medline doi:10.1126/science.aaf8060
5. H. Choi, J. Jeong, H.-B. Kim, S. Kim, B. Walker, G.-H. Kim, J. Y. Kim, Cesium-doped methylammonium lead iodide perovskite light absorber for hybrid solar cells. *Nano Energy* **7**, 80–85 (2014). doi:10.1016/j.nanoen.2014.04.017
6. J. W. Lee, D.-H. Kim, H.-S. Kim, S.-W. Seo, S. M. Cho, N.-G. Park, Formamidinium and cesium hybridization for photo- and moisture-stable perovskite solar cell. *Adv. Energy Mater.* **5**, 1501310 (2015). doi:10.1002/aenm.201501310
7. C. Yi, J. Luo, S. Meloni, A. Boziki, N. Ashari-Astani, C. Grätzel, S. M. Zakeeruddin, U. Röthlisberger, M. Grätzel, Entropic stabilization of mixed A-cation ABX_3 metal halide perovskites for high performance perovskite solar cells. *Energy Environ. Sci.* **9**, 656–662 (2016). doi:10.1039/C5EE03255E
8. Z. Li, M. Yang, J.-S. Park, S.-H. Wei, J. J. Berry, K. Zhu, Stabilizing perovskite structures by tuning tolerance factor: Formation of formamidinium and cesium lead iodide solid-state alloys. *Chem. Mater.* **28**, 284–292 (2016). doi:10.1021/acs.chemmater.5b04107
9. M. Saliba, T. Matsui, J. Y. Seo, K. Domanski, J. P. Correa-Baena, M. K. Nazeeruddin, S. M. Zakeeruddin, W. Tress, A. Abate, A. Hagfeldt, M. Grätzel, Cesium-containing triple cation perovskite solar cells: Improved stability, reproducibility and high efficiency. *Energy Environ. Sci.* **9**, 1989–1997 (2016). Medline doi:10.1039/C5EE03874J
10. D. P. McMeekin, G. Sadoughi, W. Rehman, G. E. Eperon, M. Saliba, M. T. Hörantner, A. Haghighirad, N. Sakai, L. Korte, B. Rech, M. B. Johnston, L. M. Herz, H. J. Snaith, A mixed-cation lead mixed-halide perovskite absorber for tandem solar cells. *Science* **351**, 151–155 (2016). Medline doi:10.1126/science.aad5845
11. H. L. Wells, Über die Cäsium- und Kalium-Bleihalogenide. *Z. Anorg. Chem.* **3**, 195–210 (1893). doi:10.1002/zaac.18930030124
12. D. Weber, $CH_3NH_3PbX_3$, a Pb(II)-system with cubic perovskite structure. *Z.*

Naturforsch. B **33**, 1443 (1978). doi:10.1515/znb-1978-1214

13. D. B. Mitzi, K. Liang, Synthesis, resistivity, and thermal properties of the cubic perovskite $NH_2CH{=}NH_2SnI_3$ and related systems. *J. Solid State Chem.* **134**, 376–381 (1997). doi:10.1006/jssc.1997.7593
14. G. Kieslich, S. J. Sun, A. K. Cheetham, Solid-state principles applied to organic-inorganic perovskites: New tricks for an old dog. *Chem. Sci.* **5**, 4712–4715 (2014). doi:10.1039/C4SC02211D
15. F. Hao, C. C. Stoumpos, D. H. Cao, R. P. H. Chang, M. G. Kanatzidis, Lead-free solid-state organic-inorganic halide perovskite solar cells. *Nat. Photonics* **8**, 489–494 (2014). doi:10.1038/nphoton.2014.82
16. D. M. Trots, S. V. Myagkota, High-temperature structural evolution of caesium and rubidium triiodoplumbates. *J. Phys. Chem. Solids* **69**, 2520–2526 (2008). doi:10.1016/j.jpcs.2008.05.007
17. See supplementary materials on *Science* Online.
18. J. P. Correa-Baena, M. Anaya, G. Lozano, W. Tress, K. Domanski, M. Saliba, T. Matsui, T. J. Jacobsson, M. E. Calvo, A. Abate, M. Grätzel, H. Míguez, A. Hagfeldt, Unbroken perovskite: Interplay of morphology, electro-optical properties, and ionic movement. *Adv. Mater.* **28**, 5031–5037 (2016). Medline doi:10.1002/adma.201600624
19. M. A. Green, Radiative efficiency of state-of-the-art photovoltaic cells. *Prog. Photovolt. Res. Appl.* **20**, 472–476 (2012). doi:10.1002/pip.1147
20. K. Tvingstedt, O. Malinkiewicz, A. Baumann, C. Deibel, H. J. Snaith, V. Dyakonov, H. J. Bolink, Radiative efficiency of lead iodide based perovskite solar cells. *Sci. Rep.* **4**, 6071 (2014). Medline doi:10.1038/srep06071
21. D. Bi, W. Tress, M. I. Dar, P. Gao, J. Luo, C. Renevier, K. Schenk, A. Abate, F. Giordano, J. P. Correa Baena, J. D. Decoppet, S. M. Zakeeruddin, M. K. Nazeeruddin, M. Grätzel, A. Hagfeldt, Efficient luminescent solar cells based on tailored mixed-cation perovskites. *Sci. Advances* **2**, e1501170 (2016). Medline doi:10.1126/sciadv.1501170
22. U. Rau, Reciprocity relation between photovoltaic quantum efficiency and electroluminescent emission of solar cells. *Phys. Rev. B* **76**, 085303 (2007). doi:10.1103/PhysRevB.76.085303
23. R. T. Ross, Some thermodynamics of photochemical systems. *J. Chem. Phys.* **46**, 4590 (1967). doi:10.1063/1.1840606
24. W. Tress, N. Marinova, O. Inganäs, M. K. Nazeeruddin, S. M. Zakeeruddin, M. Graetzel, Predicting the open-circuit voltage of $CH_3NH_3PbI_3$ perovskite solar cells using electroluminescence and photovoltaic quantum efficiency spectra: The role of radiative and non-radiative recombination. *Adv. Energy Mater.* **5**, 1400812 (2015). doi:10.1002/aenm.201400812
25. H. Cho, S. H. Jeong, M. H. Park, Y. H. Kim, C. Wolf, C. L. Lee, J. H. Heo, A. Sadhanala, N. Myoung, S. Yoo, S. H. Im, R. H. Friend, T. W. Lee, Overcoming the electroluminescence efficiency limitations of perovskite light-emitting diodes. *Science* **350**, 1222–1225 (2015). Medline doi:10.1126/science.aad1818
26. L. Gil-Escrig, G. Longo, A. Pertegás, C. Roldán-Carmona, A. Soriano, M. Sessolo, H. J. Bolink, Efficient photovoltaic and electroluminescent perovskite devices. *Chem. Commun.* **51**, 569–571 (2015). Medline doi:10.1039/C4CC07518H
27. G. Li, F. W. Rivarola, N. J. Davis, S. Bai, T. C. Jellicoe, F. de la Peña, S. Hou, C. Ducati, F. Gao, R. H. Friend, N. C. Greenham, Z. K. Tan, Highly efficient perovskite nanocrystal light-emitting diodes enabled by a universal crosslinking method. *Adv. Mater.* **28**, 3528–3534 (2016). Medline doi:10.1002/adma.201600064
28. N. H. Tiep, Z. L. Ku, H. J. Fan, Recent advances in improving the stability of perovskite solar cells. *Adv. Energy Mater.* **6**, 1501420 (2016). doi:10.1002/aenm.201501420
29. K. Domanski, J. P. Correa-Baena, N. Mine, M. K. Nazeeruddin, A. Abate, M. Saliba, W. Tress, A. Hagfeldt, M. Grätzel, Not all that glitters is gold: Metal-migration-induced degradation in perovskite solar cells. *ACS Nano* **10**, 6306–6314 (2016). Medline doi:10.1021/acsnano.6b02613
30. K. A. Bush, C. D. Bailie, Y. Chen, A. R. Bowring, W. Wang, W. Ma, T. Leijtens, F. Moghadam, M. D. McGehee, Thermal and environmental stability of semi-transparent perovskite solar cells for tandems enabled by a solution-processed nanoparticle buffer layer and sputtered ITO electrode. *Adv. Mater.* **28**, 3937–3943 (2016). Medline doi:10.1002/adma.201505279
31. A. Mei, X. Li, L. Liu, Z. Ku, T. Liu, Y. Rong, M. Xu, M. Hu, J. Chen, Y. Yang, M. Grätzel, H. Han, A hole-conductor-free, fully printable mesoscopic perovskite solar cell with high stability. *Science* **345**, 295–298 (2014). Medline doi:10.1126/science.1254763
32. J. H. Heo, S. H. Im, J. H. Noh, T. N. Mandal, C.-S. Lim, J. A. Chang, Y. H. Lee, H.-Kim, A. Sarkar, M. K. Nazeeruddin, M. Grätzel, S. I. Seok, Efficient inorganic-organic hybrid heterojunction solar cells containing perovskite compound and polymeric hole conductors. *Nat. Photonics* **7**, 487 (2013). doi:10.1038/nphoton.2013.80
33. Y. G. Rong, L. F. Liu, A. Y. Mei, X. Li, H. W. Han, Beyond efficiency: The challenge of stability in mesoscopic perovskite solar cells. *Adv. Energy Mater.* **5**, 1501066 (2015). doi:10.1002/aenm.201501066
34. N. Pellet, J. Teuscher, J. Maier, M. Gratzel, Transforming hybrid organic inorganic perovskites by rapid halide exchange. *Chem. Mater.* **27**, 2181–2188 (2015). doi:10.1021/acs.chemmater.5b00281
35. R. D. Shannon, Revised effective ionic-radii and systematic studies of interatomic distances in halides and chalcogenides. *Acta Crystallogr. A* **32**, 751–767 (1976). doi:10.1107/S0567739476001551
36. J. P. C. Correa Baena, L. Steier, W. Tress, M. Saliba, S. Neutzner, T. Matsui, F. Giordano, T. J. Jacobsson, A. R. Srimath Kandada, S. M. Zakeeruddin, A. Petrozza, A. Abate, M. K. Nazeeruddin, M. Grätzel, A. Hagfeldt, Highly efficient planar perovskite solar cells through band alignment engineering. *Energy Environ. Sci.* **8**, 2928–2934 (2015). doi:10.1039/C5EE02608C
37. E. Guillén, F. J. Ramos, J. A. Anta, S. Ahmad, Elucidating transport-recombination mechanisms in perovskite solar cells by small-perturbation techniques. *J. Phys. Chem. C* **118**, 22913–22922 (2014). doi:10.1021/jp5069076
38. F. Giordano, A. Abate, J. P. Correa Baena, M. Saliba, T. Matsui, S. H. Im, S. M. Zakeeruddin, M. K. Nazeeruddin, A. Hagfeldt, M. Graetzel, Enhanced electronic properties in mesoporous TiO_2 via lithium doping for high-efficiency perovskite solar cells. *Nat. Commun.* **7**, 10379 (2016). Medline doi:10.1038/ncomms10379
39. J.-Y. Seo *et al*., Ionic liquid control crystal growth to enhance planar perovskite solar cells efficiency. *Adv. Energy Mater.* 10.1002/aenm.201600767 (2016). doi:10.1002/aenm.201600767
40. C. Li, X. Lu, W. Ding, L. Feng, Y. Gao, Z. Guo, Formability of ABX_3 (X = F, Cl, Br, I) halide perovskites. *Acta Crystallogr. B* **64**, 702–707 (2008). Medline doi:10.1107/S0108768108032734

ACKNOWLEDGMENTS

M.S. conceived, designed and led the overall project. M.S., J.-Y.S., A.U., J.-P. C.-B. conducted SEM, PL and XRD experiments on the perovskite films. A.U. conducted CLSM for PL mapping. M.S., K.D. and W.T. conducted long-term aging tests on the devices. M.S., T.M., J.-P. C.-B. and A.A. prepared and characterized PV devices. A.H. participated in the supervision of the work. M.G. directed and supervised the research. M.S. wrote the first draft of the paper. All authors contributed to the discussion and writing of the paper. M.S. acknowledges support from the co-funded Marie Skłodowska Curie fellowship, H2020 Grant agreement no. 665667. A.A. received funding from the European Union's Seventh Framework Programme for research, technological development and demonstration under grant agreement no. 291771. Financial support is acknowledged from the Swiss National Science Foundation (SNSF), funding from the framework of Umbrella project (Grant Agreement Nos. 407040-153952, 407040-153990 and 200021-157135/1); the NRP 70 "Energy Turnaround"; the in the 9th call proposal 906: CONNECT PV as well as from SNF-NanoTera and Swiss Federal Office of Energy (SYNERGY). A.A. conducted IMPS experiments at the Adolphe Merkle Institute (AMI), Fribourg, Switzerland. M.G. and S.M.Z. thank the King Abdulaziz City for Science and Technology (KACST) for financial support under a joint research project. All data are available in the main paper and supplement. M.S., T.M., K.D., J.-Y.S., S.M.Z., W.T., M.G. are inventors on European Patent Application 1618056.7 submitted by École Polytechnique Fédérale de Lausanne (EPFL)/Panasonic Corporation that covers the perovskite compounds in this work.

SUPPLEMENTARY MATERIALS

www.sciencemag.org/cgi/content/full/science.aah5557/DC1
Materials and Methods

Supplementary Text
Figs. S1 to S16
Tables S1 and S2
Movie S1
References (*34*–*40*)

18 July 2016; accepted 8 September 2016
Published online 29 September 2016
10.1126/science.aah5557

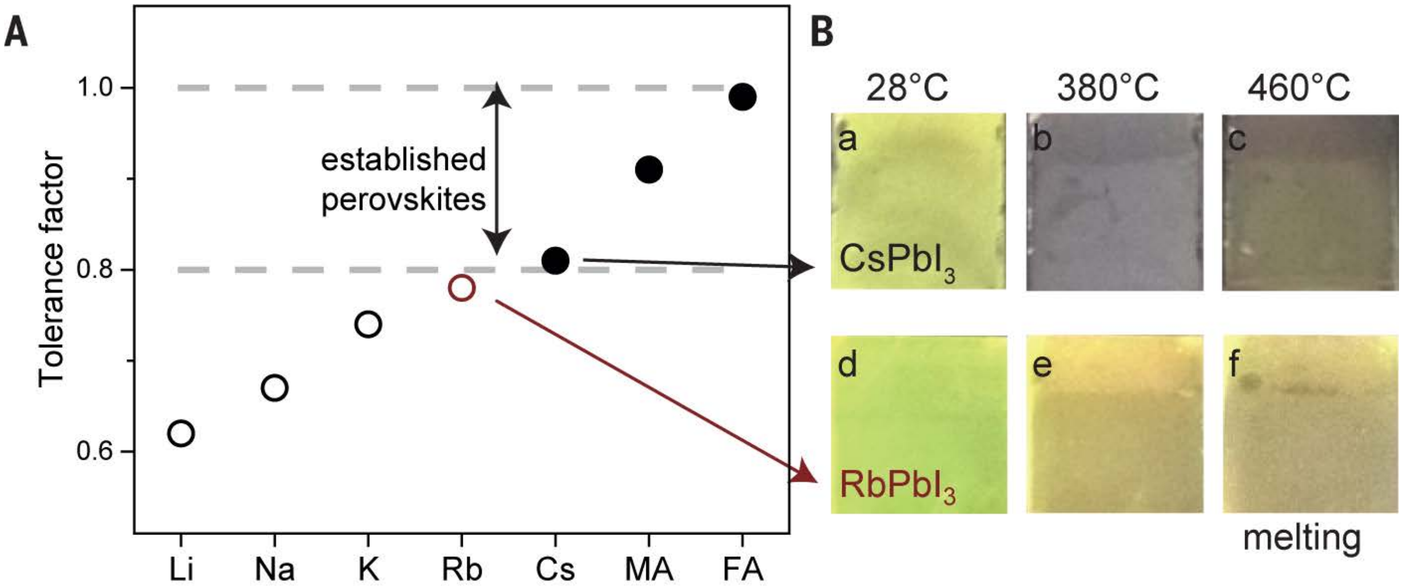

Fig. 1. Tolerance factor and perovskites at different temperatures. (**A**) Tolerance factor of $APbI_3$ perovskite with the oxidation-stable A = Li, Na, K, Rb, Cs; and MA, FA (see table S1 for detailed calculations and ionic radii). Empirically, perovskites with a tolerance factor between 0.8 and 1.0 (dashed lines) show a photoactive black phase (solid circles) as opposed to non-photoactive phases (open circles). Rb (red open circle) is very close to this limit making it a candidate for integration into the perovskite lattice. (**B**) (a-c) $CsPbI_3$ (d-f) $RbPbI_3$ at 28°C (a, d), 380°C (b, e), 460°C (c, f). Irreversible melting for both compounds occurs at 460°C. $RbPbI_3$ never shows a black phase.

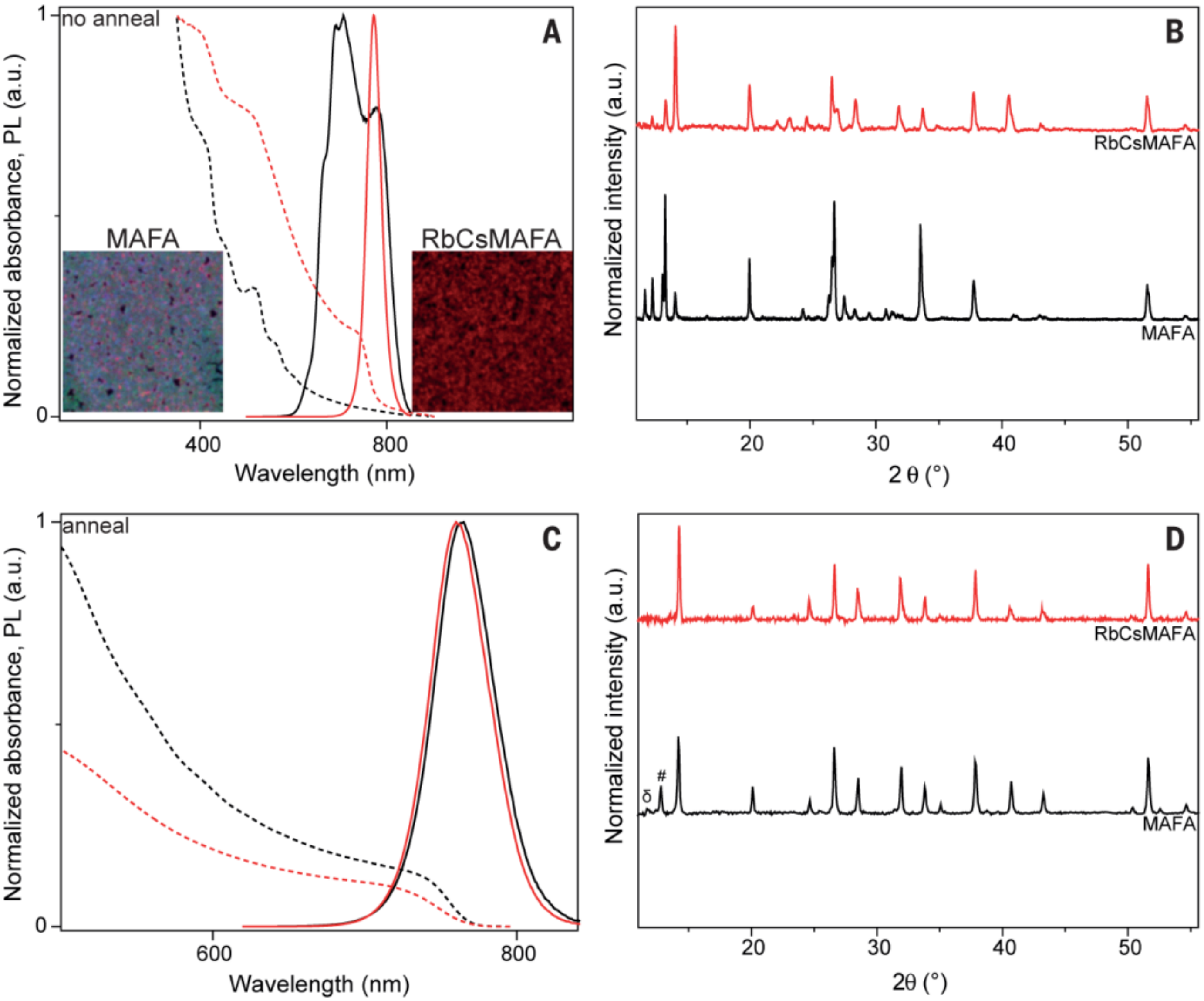

Fig. 2. Characterization of unannealed and annealed films. (**A**) UV-vis (dashed lines) and photoluminescence (solid lines) of unannealed MAFA (black) and RbCsMAFA (red) films. The inset images show fluorescence microscopy measurements (image size ~26x26 μm^2) of MAFA (left) and RbCsMAFA (right image) films. The image is an overlay of three emission ranges sampled from 640 – 650 nm, assigned as green; from 680 – 690 nm (blue); and 725 – 735 nm (red). The colors were chosen to ensure easily discernible features. (**B**) XRD data of the unannealed MAFA and RbCsMAFA films. (**C**) UV-vis (dashed) and photoluminescence (solid lines) of annealed (at 100°C for 1 hour) MAFA (black) and RbCsMAFA (red) films. (**D**) XRD data of the annealed MAFA and RbCsMAFA films. The PbI_2 and yellow phase peak is denoted as # and δ, respectively.

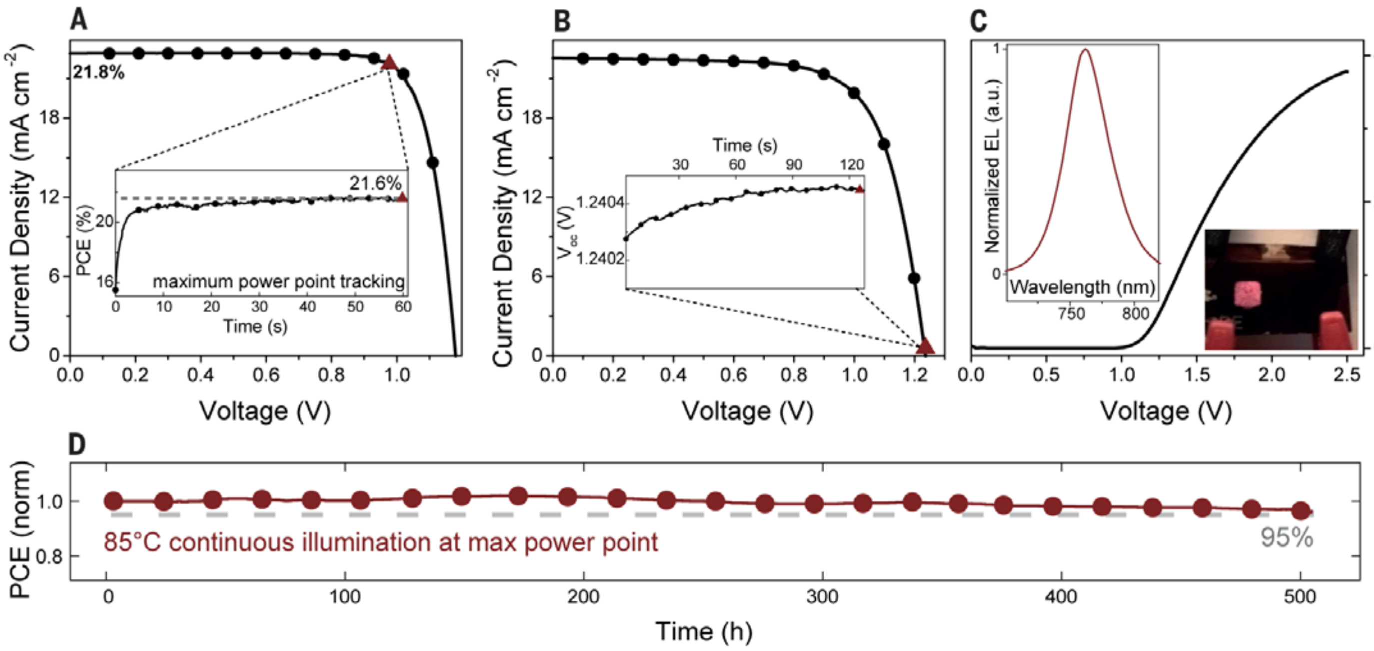

Fig. 3. Champion efficiency, open-circuit voltage, electroluminescence and high temperature stability. (**A**) Current-density/voltage (JV) curve, taken at 10 mV s^{-1} scan rate, of the best performing solar cell at 21.8% efficiency (V_{oc} = 1180 mV, J_{sc} = 22.8 mA cm^{-2}, and a fill factor of 81%). The forward and reverse scan is shown in table S2. The inset shows the scan rate independent maximum power point (MPP) tracking for 60 s resulting in a stabilized efficiency of 21.6% at 977 mV and 22.1 mA cm^{-2} (displayed as the red triangles in the JV and MPP scan, respectively). (**B**) JV curve of the highest open-circuit voltage device. The inset shows the V_{oc} over 120 s resulting in 1240 mV (displayed as the red triangles in the JV and V_{oc} scan, respectively). (**C**) EQE electroluminescence (EL) as a function of voltage. The left inset shows the corresponding EL spectrum over wavelength. The image in the inset is a solar cell with 2 active areas. The left area is operated as an LED displaying a clearly visible red emission even under ambient light. At the same time, the right area can be operated as a solar cell or a photodetector underlining the versatility of the perovskite material. (**D**) Thermal stability test of a perovskite solar cell. The device is aged for 500 hours at 85°C under continuous full sun illumination and maximum power point tracking in a nitrogen atmosphere (red curve, circles). This aging routine exceeds industry norms. During the full sun light soaking at 85°C, the device retains 95% (dashed line) of its initial performance.

Incorporation of rubidium cations into perovskite solar cells improves photovoltaic performance

Michael Saliba, Taisuke Matsui, Konrad Domanski, Ji-Youn Seo, Amita Ummadisingu, Shaik M. Zakeeruddin, Juan-Pablo Correa-Baena, Wolfgang R. Tress, Antonio Abate, Anders Hagfeldt and Michael Grätzel (September 29, 2016)

Editor's Summary

Science (print ISSN 0036-8075; online ISSN 1095-9203) is published weekly, except the last week in December, by the American Association for the Advancement of Science, 1200 New York Avenue NW, Washington, DC 20005. Copyright 2016 by the American Association for the Advancement of Science; all rights reserved. The title *Science* is a registered trademark of AAAS.